Potent neutralization of hepatitis A virus reveals a receptor mimic mechanism and the receptor recognition site

Xiangxi Wang[a,1,2], Ling Zhu[b,1], Minghao Dang[a,1], Zhongyu Hu[c,1], Qiang Gao[a,d], Shuai Yuan[a], Yao Sun[a], Bo Zhang[d], Jingshan Ren[b], Abhay Kotecha[b], Thomas S. Walter[b], Junzhi Wang[c], Elizabeth E. Fry[b,2], David I. Stuart[b,e,2], and Zihe Rao[a,f,2]

[a]National Laboratory of Macromolecules, Institute of Biophysics, Chinese Academy of Science, Beijing 100101, China; [b]Division of Structural Biology, University of Oxford, Oxford OX3 7BN, United Kingdom; [c]National Institutes for Food and Drug Control, Beijing 100050, China; [d]Sinovac Biotech Co., Ltd., Beijing 100085, China; [e]Diamond Light Sources, Didcot OX11 0DE, United Kingdom; and [f]Laboratory of Structural Biology, School of Medicine, Tsinghua University, Beijing 100084, China

Edited by Stephen P. Goff, Columbia University College of Physicians and Surgeons, New York, NY, and approved December 16, 2016 (received for review October 4, 2016)

Hepatitis A virus (HAV) infects ∼1.4 million people annually and, although there is a vaccine, there are no licensed therapeutic drugs. HAV is unusually stable (making disinfection problematic) and little is known of how it enters cells and releases its RNA. Here we report a potent HAV-specific monoclonal antibody, R10, which neutralizes HAV infection by blocking attachment to the host cell. High-resolution cryo-EM structures of HAV full and empty particles and of the complex of HAV with R10 Fab reveal the atomic details of antibody binding and point to a receptor recognition site at the pentamer interface. These results, together with our observation that the R10 Fab destabilizes the capsid, suggest the use of a receptor mimic mechanism to neutralize virus infection, providing new opportunities for therapeutic intervention.

picornavirus | entry | neutralizing mechanism | receptor recognition | uncoating

Hepatitis A virus (HAV) is an ancient and ubiquitous pathogen found in primates and small mammals (1). It is a picornavirus with many distinctive features: in the blood it is found in an enveloped form but is shed in feces as a naked, unenveloped particle (2); it possesses a low G/C ratio in the genome sequence and a strong codon bias (3); it grows poorly in tissue culture; it possesses a 67-residue carboxyl-terminal extension of VP1 (VP1-2A or VPX), which is important for viral assembly (4); and it has a very short, nonmyristoylated VP4 (∼23 residues) (5). Because of its unusual properties, HAV remains enigmatic and occupies an evolutionary position on the periphery of picornaviruses (6, 7).

Our previous crystal structure of unenveloped HAV (7) showed no trace of the canyon that encircles the fivefold axes of enteroviruses and is often the site of receptor binding (8, 9). Indeed, the structure provided no clues as to where T-cell Ig and mucin 1 (TIM-1), the proposed receptor (10, 11), might attach. In addition, the virus capsid contains no pocket factor and can withstand remarkably high temperature and low pH, indicating an uncoating mechanism (7) unlike that of enteroviruses; heating of HAV particles does not transform virions to an expanded state in vitro. Structural characterization of a HAV–TIM-1 complex might elucidate the cell-entry mechanism, but difficulty in obtaining homogenous complex preparations because of the low binding affinity of TIM-1, at least for unenveloped particles, has made this challenging. However, it is known that neutralizing antibodies (NAbs) protect against virus infection by mechanisms that include blocking attachment to the cellular receptor, overstabilizing the virus, preventing viral genome release, or physically destabilizing the virus (12, 13). Structural studies of virus complexes with such antibodies can therefore help illuminate these underlying biological functions. Here we identify a highly potent Nab, R10, which can neutralize HAV infection efficiently by blocking attachment to the host cell. The complex structure of the HAV full particle and R10 Fab suggest where the receptor may bind and, together with the ability of the R10 Fab to destabilize the capsid, point to the use of a receptor mimic mechanism to neutralize virus infection.

Results

NAb R10 Interferes with Viral Uncoating and Prevents Virus Attachment. Twenty-five monoclonal antibodies were generated by immunizing mice. Of these, the one named R10 had the strongest neutralizing activity against HAV [a 50% neutralizing concentration ($neut_{50}$) value of ∼2 nM, ∼0.3 μg/mL]. The Fab fragment is also strongly neutralizing ($neut_{50}$ = ∼3 nM, ∼0.45 μg/mL) (Fig. 1*A*). R10 does not recognize linear epitopes by immunoblot, but recognizes

Significance

Hepatitis A virus (HAV) remains enigmatic, being unusually stable physically. Where the receptor binds and how the virion can be destabilized to release the genome are unknown. We report a potent HAV-specific neutralizing monoclonal antibody, R10, that blocks receptor attachment and interferes with viral uncoating. We have determined high-resolution cryo-EM structures of HAV full particles, empty particles, and full particles complexed with R10 Fab, revealing that R10 binds to the viral surface along the edges of the pentameric building block of the virus, and these interactions are critical for receptor binding and viral uncoating. Our results point to the use of a receptor mimic mechanism to neutralize virus infection, highlighting new opportunities for therapeutic intervention.

Author contributions: X.W., E.E.F., D.I.S., and Z.R. designed research; X.W., L.Z., M.D., Z.H., Q.G., S.Y., Y.S., B.Z., T.S.W., and J.W. performed research; X.W., L.Z., M.D., Z.H., Q.G., S.Y., Y.S., B.Z., J.R., T.S.W., J.W., E.E.F., D.I.S., and Z.R. analyzed data; X.W., E.E.F., D.I.S., and Z.R. wrote the paper.

The authors declare no conflict of interest.

This article is a PNAS Direct Submission.

Freely available online through the PNAS open access option.

Data deposition: The atomic coordinates of hepatitis A virus (HAV) empty particle, HAV full particle, NAb R10 Fab, and HAV full particle:R10 Fab have deposited in the Protein Data Bank, www.pdb.org (PDB ID codes 5WTF, 5WTE, 5WTG, and 5WTH, respectively). Cryo-EM density maps of HAV empty, full particle, and full particle complexed with R10 Fab have been deposited with the Electron Microscopy Data Bank, https://www.ebi.ac.uk/pdbe/emdb (EMD ID codes EMD-6687, EMD-6686, and EMD-6688, respectively).

[1]X.W., L.Z., M.D., and Z.H. contributed equally to this work.

[2]To whom correspondence may be addressed. Email: xiangxi@ibp.ac.cn, liz@strubi.ox.ac.uk, dave@strubi.ox.ac.uk, or raozh@xtal.tsinghua.edu.cn.

This article contains supporting information online at www.pnas.org/lookup/suppl/doi:10.1073/pnas.1616502114/-/DCSupplemental.

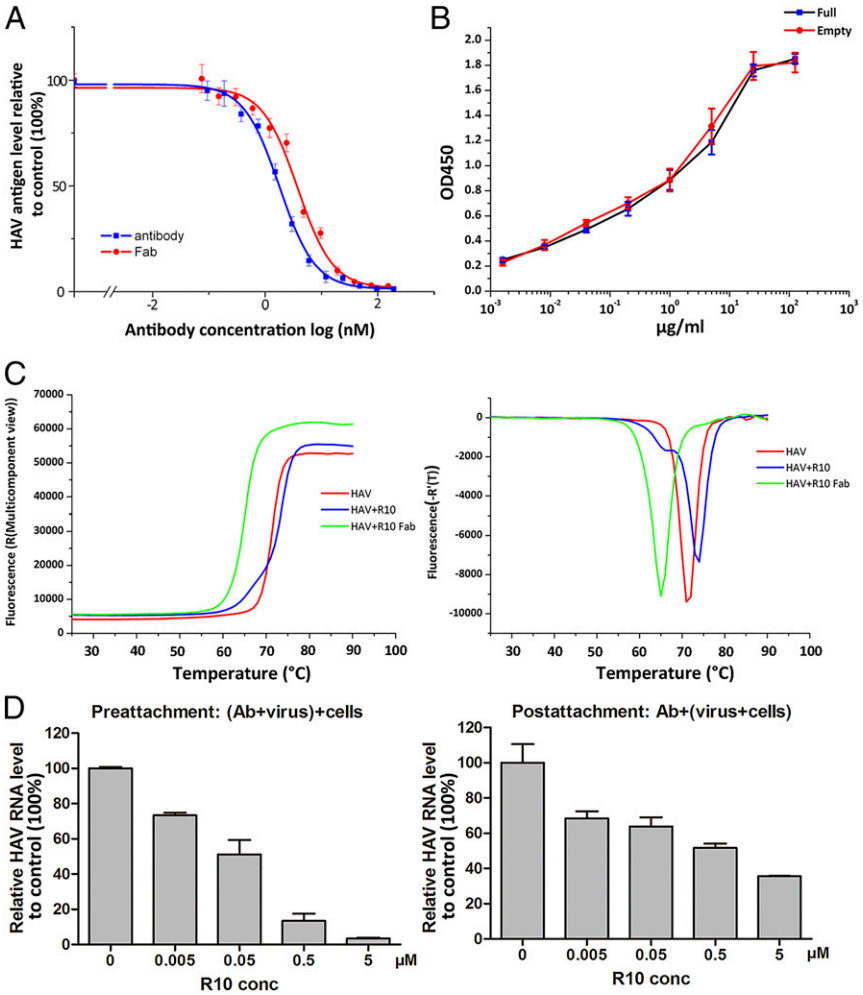

Fig. 1. Characterizations of the monoclonal antibody R10. (*A*) Neutralization of HAV by R10. Whole Ig G and Fab fragments of R10 were used to block HAV infection at different concentrations by detecting HAV capsids. The red and blue symbols and curves represent whole antibody and Fab fragments, respectively. HAV capsids were measured by indirect ELISA and the values are mean from triplicate wells with the SD. (*B*) Analysis of binding of R10 to HAV mature virions and empty particles by ELISA: 96-well plates were coated with HAV full or empty particles and various concentrations of R10 were added. The amount of bound R10 was detected by HRP assay (*SI Materials and Methods*) and the parameter on the *x* axis represents the concentrations of R10; the average OD450 readings from triplicate wells at each dilution with the SD are shown. (*C*) The stabilities of HAV full particles and their complexes with R10 whole Ig G and Fab fragments at neutral pH were determined by thermofluor assay using the dye SYTO9 to detect RNA exposure (32). The raw fluorescence traces (*Left*) are shown for HAV full particles (red line) as well as their complexes with R10 whole Ig G (blue line) and Fab fragments (green line) following incubation with SYTO9, and their first derivatives are shown (*Right*). (*D*) Amount of virus on the cell surface, as detected by RT-PCR, when exposed to R10 before (*Left*) and after (*Right*) the virus was allowed to attach to cells. High concentrations of R10 prevent attachment of HAV to the cell surface when HAV is exposed to R10 before cell attachment and R10 can strip HAV off the cell surface when HAV is exposed to R10 postattachment. Values are mean ± SD. Experiments were repeated in triplicate.

conformational epitopes by ELISA, and shows similar binding affinities to full and empty particles (Fig. 1*B*). Interestingly, a fluorescent assay revealed that whereas the R10 Fab portion destabilizes full HAV particles by 7 °C, the intact R10 stabilizes the particles by 2 °C (Fig. 1*C* and Fig. S1*A*). The same assay indicates that the bivalent intact antibody induces a two-stage transition in protein conformation to release the RNA genome (Fig. 1*C* and Fig. S1*A*). The first event, producing a slight exposure of RNA, occurs at a similar temperature to that seen with the Fab, whereas the second, which fully exposes the genome (Fig. 1*C* and Fig. S1*B*), occurs at a slightly higher temperature than in the unliganded virus, presumably because of the two arms of the antibody holding the particles together. The TIM-1 Ig V domain alone has no effect on viral stability in thermofluor assays (Fig. S1*C*). This observation is consistent with previous reports, which conclude that although the TIM-1 Ig V domain is necessary for binding of HAV, both the TIM-1 Ig V and mucin domains are required to trigger uncoating of HAV (14). Unlike foot and mouth disease virus, where uncoating is initiated at low pH, HAV exhibits an extremely robust conformation at low pH (pH 5.0), even after R10 binding (Fig. S1*C*), suggesting that an acidic environment might not be essential for HAV uncoating. Note that the HAV particles do not start to uncoat at physiological temperatures even after destabilization by Fab. They continue to exist as mature virions and remain stable as most picornaviruses, so that destabilization is unlikely to be the neutralization mechanism. For HAV, the mechanism of RNA genome release remains unclear and it is possible that a cellular receptor or a specific host factor may be required for particle disassembly. Given the ability of the R10 Fab to destabilize HAV, the binding sites on HAV of the host factor and R10 may overlap partially or fully. To explore the mechanism of neutralization, real-time RT-PCR was carried out to quantify the virus remaining on the cell surface, following exposure to antibodies pre- and postvirus attachment to cells at 4 °C. The results suggest that R10 prevents HAV attachment to the cell surface and is able to displace virus that has already bound to the cell receptor (Fig. 1*D*). In addition, R10 competitively blocked TIM-1 Ig V binding to HAV (Fig. S2 *A* and *B*), consistent with R10 preventing HAV from attaching to host cells by blocking the binding of HAV to TIM-1.

Structure Determination. Cryo-EM micrographs of the previously characterized (7) full and empty formaldehyde-inactivated HAV genotype TZ84 (HAV IA) particles and the R10 Fab:full particle complex were recorded using an FEI Polara electron microscope equipped with a Gatan K2 Summit detector (Fig. S3 *A*–*C*). The structures of the HAV full particle, empty particle, and the R10 Fab:full particle complex were determined at resolutions of 3.4, 3.8, and 4.2 Å with 4,587, 4,393, and 1,752 particles, respectively, by single-particle techniques using the "gold" standard Fourier shell correlation (FSC) = 0.143 criterion (15) (Fig. S3 *D*–*G*). At 3.4- and 3.8-Å resolution, the cryo-EM electron density maps of the full and empty particles are well resolved for the most part, allowing us to place the X-ray structures (7) in the maps (Fig. S4) and then optimize and validate them using standard X-ray crystallographic-derived methods (16) (Table S1). In addition, the crystal structure of the isolated NAb Fab R10 was

determined at a resolution of 2.9 Å (Table S2). The 4.2-Å cryo-EM map of the R10 Fab:full particle complex clearly reveals the polypeptide backbone, many bulky side chains, and the mode of pathogen–antibody interaction (Fig. S4). To define precisely the atomic determinants of the interaction, the refined cryo-EM structure of the HAV full particle (3.4 Å) and crystal structure of the R10 Fab (2.9 Å) were fitted into the EM map and then refined against the phased structure factors calculated from the 4.2-Å EM map in Phenix (16).

Cryo-EM Structures of HAV Full Particles and Empty Particles. The full and empty particles have indistinguishable external surfaces (Fig. 2 *A*–*C*), consistent with the similar binding affinities of R10 to the two types of particle (Fig. 1*B*). Major differences are seen in internal structures, many of which were previously seen when comparing the X-ray structures (7), including disordering of the N-terminal ∼40 residues of VP1 and ∼20 residues of VP0 around the threefold axes in the empty particle (Fig. 2*E*). However, the EM map reveals clearer density for the RNA genome in the full particles, where it appears as multiple layers with visible contacts with the inner capsid (Fig. 2*D*). In picornaviruses, the single-stranded RNA genome is highly condensed and packed at >800 mg/mL (17), double the concentration of the dsRNA *Reoviridae* (18), for example, but the organization in picornaviruses has proved difficult to visualize. The layered structure we observe in HAV is slightly reminiscent of that observed in other virus families (18).

Structure of HAV Full Particles in Complex with NAb R10 Fab. Understanding the structural basis of how R10 Fab prevents receptor binding and destabilizes HAV (Fig. 1) may help resolve the enigma of how this virus, which is stable up to 80 °C and to extremes of pH, uncoats. The level of electron density for the Fab suggests that all or almost all of the possible 60 copies are attached to each virus particle (Fig. 3 *A* and *B*). HAV capsid proteins exhibit no notable conformational changes upon binding to R10 Fab with an rmsd of 0.2 Å between the R10 Fab bound and unbound states of HAV. R10 binds to the viral surface along the edges of the pentameric building block of the virus, between the twofold and threefold axes in a similar position to that observed for AM28 antibody bound to parecho virus and NAb E18 binding to EV71 (13, 19) (Fig. 3 *C* and *D* and Fig. S5). Specifically, the Fab binds across the interface between pentamers, interacting with VP2 (interaction area 300 Å^2) and VP3′ from different pentamers (interaction area 753 Å^2) (Fig. 3*E* and Fig. S6 *A* and *B*). This epitope is only 18 Å from the nearest twofold axis and we note that in enteroviruses, the twofold axes separate during the initial stage of uncoating (20), so antibodies binding in this region might either prevent uncoating or catalyze premature uncoating. Indeed, R10 Fab destabilizes HAV by 7 °C, although a temperature of over 60 °C is still required to trigger uncoating, so that whereas Fab binding will not trigger uncoating at physiological temperatures, binding appears to favor a structure en route to uncoating. In contrast, intact R10 slightly inhibits full uncoating, possibly by cross-linking pentamers.

The NAb R10 Epitope. The heavy-chain and light-chain variable domains contribute ∼60% and ∼40% of the protein–protein interface, respectively, with the heavy chain predominantly binding VP3, whereas the light chain binds VP2 and VP3 (Fig. S6 *A* and *B*). The interaction surface on R10 comprises four of the six common complementary determining regions (CDRs): H1 (residues 28–32), H2 (residues 52–57), H3 (residues 100–106), and L1 (residues 30–31) with, unusually, additional interactions contributed by the light-chain framework region (L1-2, residues 45–55) (Fig. 4*A* and Fig. S6 *A* and *B*). The epitope on HAV includes residues 64–71 of VP2 and residues 68–78, 143–150, 209, and 246 of VP3 (Fig. 4*A* and Table S3). Residues comprising the epitope are 87.5% identical and 91.7% conserved across six human HAV genotypes (Fig. S6 *C* and *D*), suggesting that R10 is likely to be bind strongly to most human HAVs. Tight binding is facilitated by 19 hydrogen bonds, the antibody components of these include the side-chain of Y48 (L-chain), and main-chain carbonyl groups of V103 (H-chain) and L53 (L-chain), which interact with K150 (VP3) and R209 (VP3), respectively, and indirectly with R67 (VP2) (Fig. 4*A*).

NAb R10 May Be a Receptor Mimic. Interestingly, Fab binding displaces a string of sulfate ions bound to positive charges, notably R67 of VP2 and K150 and R209 of VP3, which fringe the pentameric assemblies (Fig. 4*B*) (7), an area predicted to bind the protein or glycans of TIM-1. To test this idea, we investigated whether sulfated glycans can inhibit HAV infection and found that heparin significantly inhibited HAV infection in a dose-dependent manner (Fig. 4*C*), consistent with TIM-1 facilitating cell entry by attachment of its highly glycosylated mucin-like region to HAV in this region (14). The extracellular portion of TIM-1 contains an N-terminal Ig variable-like (Ig) domain (d1) followed by a mucin-like region. The Ig-like d1 is required for binding of HAV, but without the mucin-like region, soluble d1 binds and neutralizes HAV inefficiently (14). d1 shares some structural similarity with both the VH and VL domains of R10 Fab but is much more similar to the VL domain (rmsds for 89.3% and 95.4% of Cαs are 5.3 Å and 3.4 Å for VH and VL,

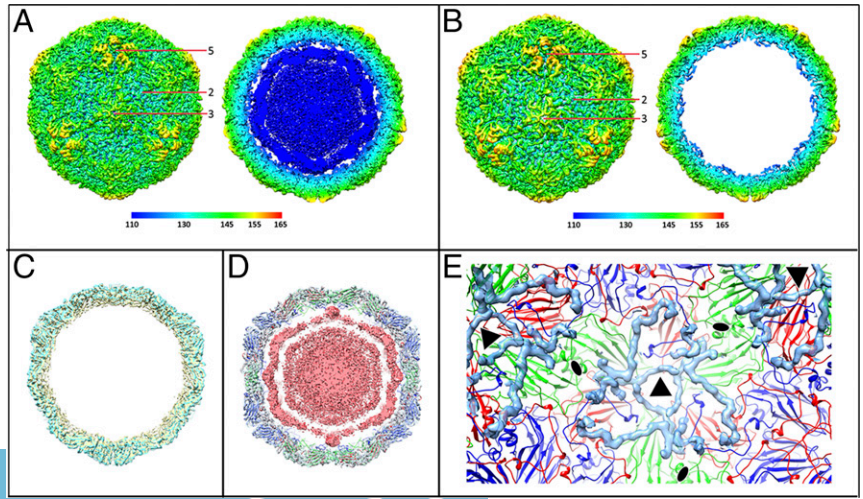

Fig. 2. Structural comparisons of HAV full and empty particles. Three-dimensional reconstructions of HAV full particle (*A*) and empty particle (*B*) viewed down a threefold axis. The central sections of HAV full and empty particles viewed along a fivefold axis are shown in the right panel of *A* and *B*, respectively. The surface is colored by radius from blue to red. The icosahedral fivefold, threefold, and twofold axes are labeled as 5, 3, and 2, respectively. (*C*) Superposition of capsid maps of HAV full (pale yellow) and empty (cyan) particles shows indistinguishable external surfaces. (*D*) Approximately 20-Å-thick slabs of the full particle reconstruction viewed along a twofold axis, with the coordinates of the HAV full particle structure [shown as a cartoon colored as VP1 (blue), VP2 (green), and VP3 (red)]. The densities corresponding to HAV capsids and genome are colored in gray and salmon, respectively. (*E*) HAV viewed from inside. Cyan density derived by subtracting the map of the empty particle (with correct scale) from the map of the full particle shows that the N-termini of VP1 and VP2 are well defined, stabilized by RNA in the full particle.

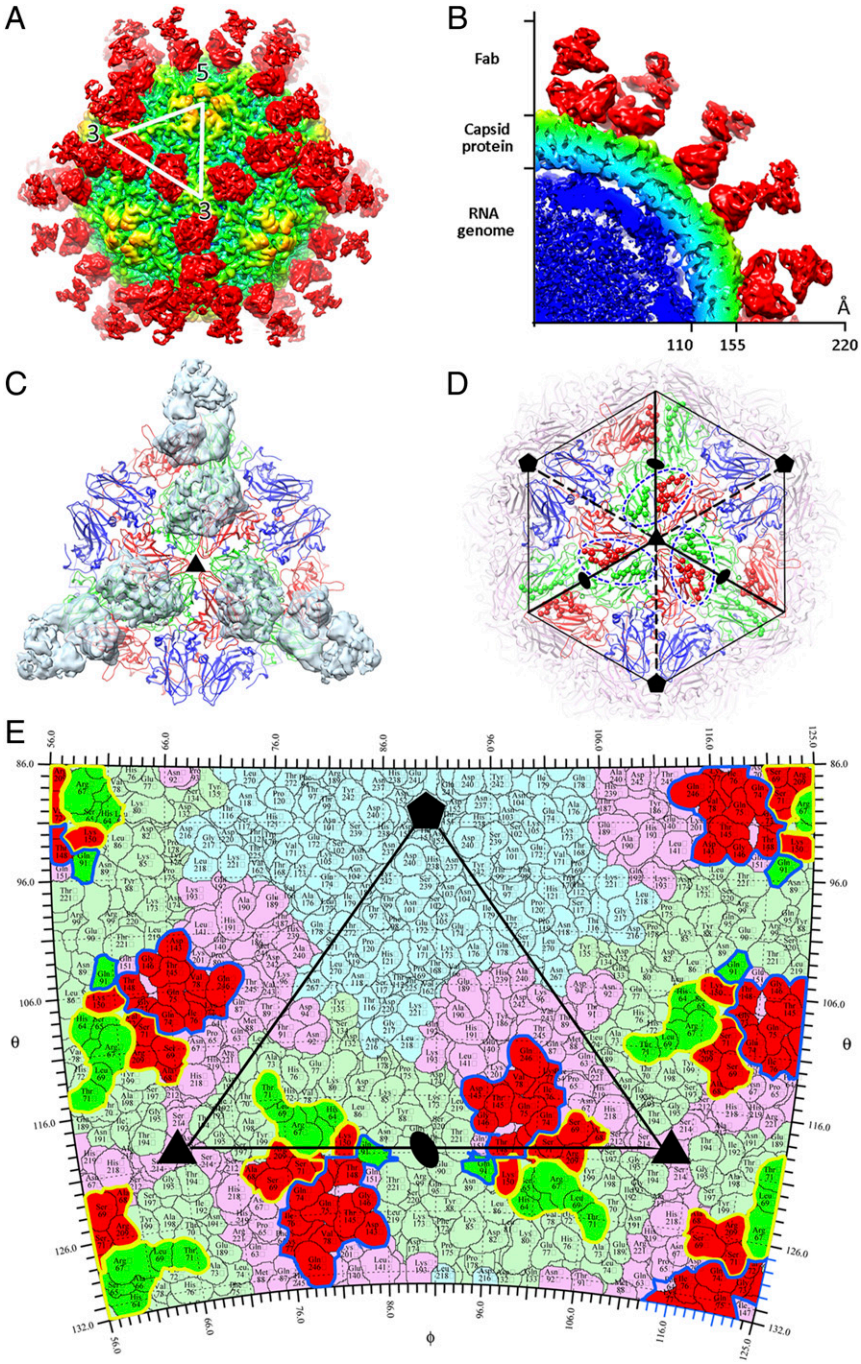

Fig. 3. The 4.2-Å resolution cryo-EM structure of the R10 Fab:HAV full-particle complex. The surface (*A*) and the cross section (*B*) of the cryo-EM map. One icosahedral asymmetric unit is indicated by a white triangle. (*C*) The R10 Fab binds to the viral surface along the pentamer interface between the twofold and threefold axes. (*D*) The R10 epitopes on six asymmetric units of the HAV surface. VP1, VP2, and VP3 are colored in blue, green, and red, respectively; residues interacting with heavy and light chains of the Fab are shown as spheres. The boundary of each epitope is marked with a deep blue dashed ellipse. Positions of five-, three-, and twofold icosahedral symmetry axes are marked as pentagons, triangles, and ovals, respectively. (*E*) The R10 footprints on the HAV surface. The figure shows a 2D projection of the HAV surface produced using RIVEM (44). Residues of VP1, VP2, and VP3 are outlined in pale blue, green, and red, respectively; residues involved in binding to R10 are shown in brighter colors corresponding to the protein chain they belong to. The footprints of R10 heavy and light chains are indicated by blue and yellow lines respectively. Five-, three-, and twofold icosahedral symmetry axes are marked as for *D* on one icosahedral asymmetric unit.

respectively) (Fig. S2 *C* and *D*). Furthermore, the major point of interaction of the VH domain is in the extended CDR3 region, which has no structural similarity in d1; the major interactions with the VL domain are with the framework region. Thus, not only is the VL domain similar to d1 of TIM-1, but it interacts with the virus via a region that is not usually part of the antibody binding site, but can be part of the adhesion surface in Ig-like adhesion molecules (21). It is therefore possible that TIM-1 binding to HAV involves d1 attachment via interactions that recapitulate the R10 VL contacts, with additional affinity conferred by interactions with the mucin-like domain. The much weaker binding of TIM-1 than R10 is consistent with much of the R10 affinity deriving from VH interactions, although assays of TIM-1 binding generally use *Escherichia coli*-expressed material lacking the mucin-like domain, and so underestimate the strength of interaction. Nevertheless it is unlikely that attachment of a relatively small number of receptors could, alone, trigger uncoating of the very robust HAV particles.

Discussion

Uncoating—release of the viral genome into the host-cell cytosol—is key to picornavirus infection. Among picornaviruses, the process is best understood for enteroviruses, where uncoating is thought to proceed via expanded intermediate particles, which have been captured for structural analysis (20). In contrast aphtho- and cardioviruses appear to simply dissociate into pentamers (22), although an unidentified intermediate particle, facilitating directed egress of the RNA, cannot be ruled out. In both cases the loss of

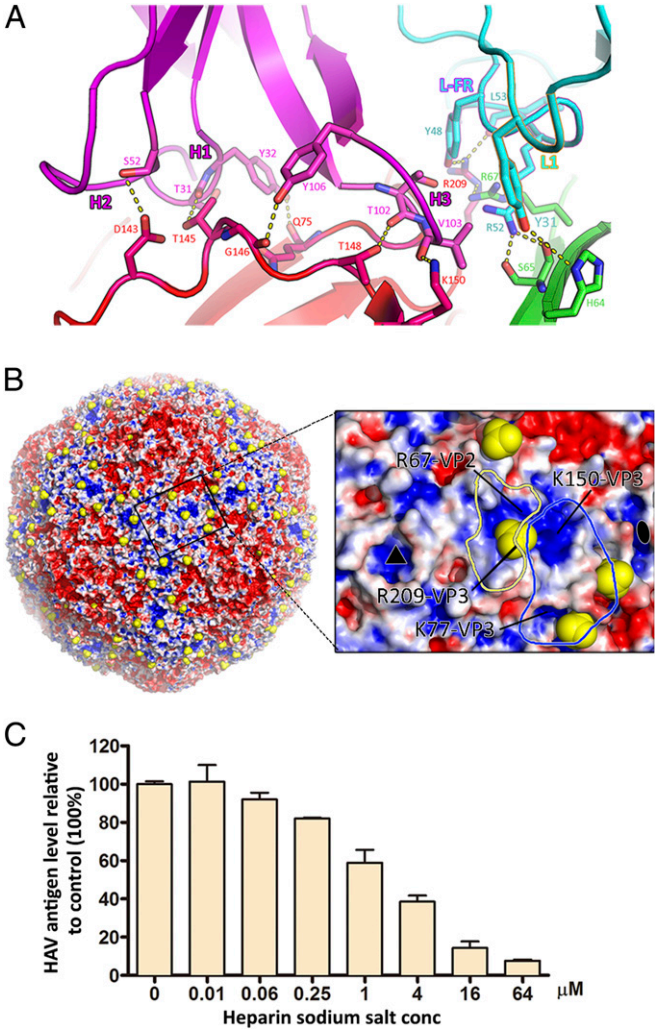

Fig. 4. R10 occupies the positively charged region of HAV surface where glycans on the potential receptors might attach. (*A*) Interaction between R10 Fab and HAV capsid proteins. Some residues involved in the formation of hydrogen bonds are shown as sticks and labeled. VP2, VP3, light-chain, and heavy-chain are colored in green, red, cyan, and magenta, respectively. Three CDRs of the heavy chain and epitope on VP2 and VP3 are highlighted by black outlines. The CDR1 and framework region of the light chain are highlighted by orange and purple outlines, respectively. (*B*) HAV electrostatic surface (calculated using APBS in PyMOL). Red, blue, and white represent negative, positive, and no charges, respectively. Yellow spheres mark the positions of bound sulfates in the X-ray structure (7). (*Right*) Close up. Regions correlated with the R10 heavy- and light-chain binding sites are indicated by blue and yellow lines, respectively. Residues that dominate the positively charged surface, as well as interacting with R10, are labeled. (*C*) Dose-dependent inhibition of HAV infection by heparin. Various concentrations of heparin were preincubated with HAV for 1 h at room temperature before infection of 2BS cells. The inhibitory ability of the sodium salt of heparin was evaluated by determining HAV antigen content using indirect ELISA. Values are mean ± SD. Experiments were repeated in triplicate.

interactions at the icosahedral twofold axes is a crucial step. Indeed these regions can be targeted to overstabilize the virus capsid, for example by capsid engineering for improved vaccines (23), or to destabilize the capsid: for example, NAb E18 binds here and causes ejection of the genome from enterovirus EV71 (13). We have found that the potent NAb R10 Fab binds in this region and somewhat destabilizes the particles, consistent with HAV uncoating also proceeding via changes at the pentamer interface. Furthermore, we find evidence that the TIM-1 receptor also binds in this region, perhaps using interactions resembling those seen for the light chain of the R10 Fab. Neutralization is therefore presumably by preventing receptor binding. In summary, our results demonstrate how increasing access to panels of authentic neutralizing monoclonal antibodies will facilitate structure–function studies to unpick the underlying biological processes of viral–host interactions, and will also provide new opportunities for therapeutic intervention.

Materials and Methods

Particle Production and Purification. HAV virus genotype TZ84 was propagated in 2BS cells at a multiplicity of infection (MOI) of 0.2 at 33–34 °C. Particle production and purification have been described previously (7). All animal procedures were carried out in accordance with the guideline for the Use of Animals in Research issued by the Institute of Biophysics, Chinese Academy of Sciences.

Crystallization, Data Collection, and Structure Determination. Purified Fab was concentrated to 8 mg/mL, and crystallization screening carried out using the sitting-drop vapor diffusion method in 96-well plates (24). Cubic crystals appeared in 20% (wt/vol) PEG3350, 0.2 M sodium thiocyanate within 2 wk. Cryo-cooling was carried out by soaking a crystal in reservoir solution containing 20% (vol/vol) glycerol and X-ray data were collected at I03, Diamond Light Source. Diffraction images (exposure time 0.1 s with 40% beam transmission) of 0.1° rotation were recorded on a PILATUS 6M detector, at a wavelength of 0.9765 Å to a resolution of 2.9 Å.

Data were processed, integrated, and scaled using the HKL2000 package (25). The crystal belongs to space group *P*21 with cell parameters $a = 52.5$ Å, $b = 140.5$ Å, $c = 68.9$ Å, $\alpha = 90°$, $\beta = 110°$, $\gamma = 90°$. Structure determination by molecular replacement with a Fab search model [PDB ID code 1QGC (26)] used the program PHASER (27). Manual model building and refinement were performed with COOT (28) and PHENIX (29). Data collection and structure refinement statistics are given in Table S2.

Thermofluor Assay. Thermofluor experiments were performed with an MX3005p RT-PCR instrument (Agilent). SYTO9 and SYPRO red (both Invitrogen) were used as fluorescent probes to detect the presence of single-stranded RNA and exposed hydrophobic regions of proteins, respectively (30–32). Fifty-microliter reactions were set up in a thin-walled PCR plate (Agilent), containing 1.0 μg of either virus or 1.0 μg of virus plus 3.0 μg of R10 antibody (~120 R10 molecules per HAV virion), or 1.0 μg of virus plus 2.0 μg of R10 Fab (~240 R10 Fab molecules per HAV virion), or 1.0 μg of virus plus 0.5 μg of TIM-1 Ig V (~240 TIM-1 Ig V molecules per HAV virion), 5 μM SYTO9 and 3× SYPRO red in PBS buffer solutions, and ramped from 25 to 99 °C with fluorescence recorded in triplicate at 1 °C intervals. The RNA release (Tr) and melting temperature (Tm) were taken as the minima of the negative first derivative of the RNA exposure and protein denaturation curves, respectively.

RT-PCR to Quantitate Virus on the Cell Surface. The amount of HAV remaining on the surface of 2BS cells after R10 treatment was estimated by quantitative RT-PCR, as previously described (33). In brief, HAV was mixed with different concentrations of R10 before and after the virus attached to cells (MOI of ~1) at 4 °C. The cells were washed three times and total cellular RNA purified using RNeasy mini kit (Qiagen), as described in the manufacturer's instructions. Real-time quantitative PCR (qPCR) was performed using One Step SYBR PrimeScript RT-PCR Kit (TaKaRa) in a CFX 96 Real-Time System (Bio-Rad). The 25-μL reaction contained 12.5 μL 2× One Step SYBR RT-PCR Buffer III, 0.5 μL TaKaRa Ex Taq HS, 0.5 μL PrimeScript RT Enzyme Mix II, 0.5 μL each of 10 μM forward (5′-TGG AAT CAC ATT AAA GCA AGC AA-3′) and reverse primers (5′-GGA ACA CGA AAT CTC AAA GTT GAC T-3′), 2 μL total RNA, and 8.5 μL RNase-free H_2O. The thermal profile for qPCR was 42 °C for 5 min for reverse transcription, 95 °C for 10s for reverse transcription inactivation; this was followed by 40 cycles of denaturation at 95 °C for 10 s, annealing and extension at 60 °C for 30 s. GAPDH was used as the housekeeping gene to normalize samples (forward 5′-CTG TTG CTG TAG CCA AAT TCGT-3′, reverse 5′-ACC CAC TCC TCC ACC TTT GAC-3′). The analysis of relative levels of HAV RNA in different samples was performed by comparative $2^{-\Delta\Delta CT}$ method (34).

TIM-1 Ig V Domain Expression and Purification. Human TIM-1 Ig V domain (residues 22–129, d1) was cloned in a pET-22b vector (Novagen) with a C-terminal 6×His-tag and expressed in *E. coli* Bl21 (DE3). Soluble receptor domain was prepared from inclusion bodies by in vitro refolding, purified, and activity checked as described previously (11).

Cryo-EM and Data Collection. Purified R10 Fab fragments were incubated with HAV full particles (at a concentration of ~1 mg/mL) at room temperature for 1 h at a ratio of five Fab fragments per icosahedral asymmetric unit of the virus. A 3-μL aliquot of purified HAV full or empty particles or the mixture of full particles and R10 Fab (~1, 0.8, and 1 mg/mL, respectively) was applied to a freshly glow-discharged 400-mesh holey carbon-coated copper grid (C-flat, CF-2/1–2C, Protochips). Grids were blotted for 2.5 s in 80% relative humidity for plunge-freezing (Vitrobot; FEI) in liquid ethane. Cryo-EM datasets were collected at 300 kV with an FEI Tecnai G2 Polara microscope (FEI), equipped with a GIF Quantum energy filter (Gatan) operated in zero energy-loss mode with a slit width of 20 eV, and direct electron detector (K2 Summit; Gatan). Movies (25 frames, each 0.2 s, total dose 25 e^{-} $Å^{-2}$) were recorded with a defocus between 1.2 and 2.8 μm in single electron counting mode using SerialEM (35).

Image Processing, 3D Reconstruction, Model Building, and Refinement. The frames from each movie were aligned and averaged for the correction of beam-induced drift using MOTIONCORR (36). Particles from micrographs were picked automatically using ETHAN (37) and then manually screened using the boxer program in EMAN (38). The CTF parameters for each micrograph were estimated by using a GPU accelerated program Gctf (39). Cryo-EM structures were determined with Relion 1.3 (40) with the application of icosahedral symmetry. The crystal structure of the HAV full particle [PDB ID code 4QPI (7)], low-pass–filtered to 40 Å, was used as an initial model for 3D classification and refinement. For the complex of full particle and Fab, the initial model was created by EMAN2 (41). A total of 4,587 HAV full particles, 4,393 empty particles, and 1,752 complex particles were used to obtain the final density maps at 3.4, 3.8, and 4.2 Å respectively, as evaluated by the so-called "gold standard" FSC procedure between two half maps (threshold = 0.143). The crystal structure of HAV full particle [PDB ID code 4QPI (7)] was used to fit the HAV full particle, empty particle, and complex EM maps. Initial fitting was done manually using the program CHIMERA (42) and then optimized using the "Fit in Map" function in CHIMERA. The fit was further improved with real-space refinement with COOT (28). Fitting of the crystal structure of the R10 Fab molecules was done similarly. All three models were further refined by positional and B-factor refinement in real space using Phenix (16) and rebuilding in COOT (28) iteratively. The final models were evaluated by Molprobity (43) functions integrated in Phenix. Data and refinement statistics are summarized in Table S1.

Full experimental details are available in *SI Materials and Methods*.

ACKNOWLEDGMENTS. We thank Jun Dong and Jonathan Diprose for IT support and the Oxford Particle Imaging Centre electron microscopy facility and the Center for Biological imaging, Institute of Biophysics for electron microscopy work. Work was supported by the Ministry of Science and Technology 973 Project (Grant 2014CB542800); National Science Foundation Grants 81330036, 31570717, 81621005, and 81520108019; the Strategic Priority Research Program of the Chinese Academy of Sciences Grant XDB08020200; National Key Research and Development Project of China (2016YFD0500304); and Medical Research Center Grants G100099 and MR/N00065X/1. The work of the Wellcome Trust Centre in Oxford is supported by the Wellcome Trust Core Award 090532/Z/07/Z. X.W. was supported by a Young Elite Scientist sponsorship by the China Association for Science and Technology. The Oxford Particle Imaging Centre electron microscopy facility was founded by Wellcome Trust JIF Award 060208/Z/00/Z and is supported by Wellcome Trust Equipment Grant 093305/Z/10/Z.

1. Drexler JF, et al. (2015) Evolutionary origins of hepatitis A virus in small mammals. *Proc Natl Acad Sci* 112(49):15190–5.
2. Feng Z, et al. (2013) A pathogenic picornavirus acquires an envelope by hijacking cellular membranes. *Nature* 496(7445):367–371.
3. Aragonès L, Guix S, Ribes E, Bosch A, Pintó RM (2010) Fine-tuning translation kinetics selection as the driving force of codon usage bias in the hepatitis A virus capsid. *PLoS Pathog* 6(3):e1000797.
4. Cohen L, Bénichou D, Martin A (2002) Analysis of deletion mutants indicates that the 2A polypeptide of hepatitis A virus participates in virion morphogenesis. *J Virol* 76(15):7495–7505.
5. Tesar M, Jia XY, Summers DF, Ehrenfeld E (1993) Analysis of a potential myristoylation site in hepatitis A virus capsid protein VP4. *Virology* 194(2):616–626.
6. Rowlands DJ (2015) Human hepatitis A virus is united with a host of relations. *Proc Natl Acad Sci* 112(49):15010–1.
7. Wang X, et al. (2014) Hepatitis A virus and the origins of picornaviruses. *Nature* 517:(7532):85–8.
8. Dang M, et al. (2014) Molecular mechanism of SCARB2-mediated attachment and uncoating of EV71. *Protein Cell* 5(9):692–703.
9. Wang X, et al. (2012) A sensor-adaptor mechanism for enterovirus uncoating from structures of EV71. *Nat Struct Mol Biol* 19(4):424–429.
10. Kaplan G, et al. (1996) Identification of a surface glycoprotein on African green monkey kidney cells as a receptor for hepatitis A virus. *EMBO J* 15(16):4282–4296.
11. Yuan S, et al. (2015) TIM-1 acts a dual-attachment receptor for Ebolavirus by interacting directly with viral GP and the PS on the viral envelope. *Protein Cell* 6(11):814–824.
12. Lin J, et al. (2012) Structure of the Fab-labeled "breathing" state of native poliovirus. *J Virol* 86(10):5959–5962.
13. Plevka P, et al. (2014) Neutralizing antibodies can initiate genome release from human enterovirus 71. *Proc Natl Acad Sci USA* 111(6):2134–2139.
14. Silberstein E, et al. (2003) Alteration of hepatitis A virus (HAV) particles by a soluble form of HAV cellular receptor 1 containing the immunoglobin-and mucin-like regions. *J Virol* 77(16):8765–8774.
15. Scheres SH, Chen S (2012) Prevention of overfitting in cryo-EM structure determination. *Nat Methods* 9(9):853–854.
16. Afonine PV, et al. (2012) Towards automated crystallographic structure refinement with phenix.refine. *Acta Crystallogr D Biol Crystallogr* 68(Pt 4):352–367.
17. Kuznetsov YG, Daijogo S, Zhou J, Semler BL, McPherson A (2005) Atomic force microscopy analysis of icosahedral virus RNA. *J Mol Biol* 347(1):41–52.
18. Gouet P, et al. (1999) The highly ordered double-stranded RNA genome of bluetongue virus revealed by crystallography. *Cell* 97(4):481–490.
19. Shakeel S, et al. (2015) Structural basis of human parechovirus neutralization by human monoclonal antibodies. *J Virol* 89(18):9571–9580.
20. Ren J, et al. (2013) Picornavirus uncoating intermediate captured in atomic detail. *Nat Commun* 4:1929.
21. Springer TA, Wang J-H (2004) The three-dimensional structure of integrins and their ligands, and conformational regulation of cell adhesion. *Adv Protein Chem* 68:29–63.
22. Cavanagh D, Rowlands DJ, Brown F (1978) Early events in the interaction between foot-and mouth disease virus and primary pig kidney cells. *J Gen Virol* 41(2):255–264.
23. Kotecha A, et al. (2015) Structure-based energetics of protein interfaces guides foot-and-mouth disease virus vaccine design. *Nat Struct Mol Biol* 22(10):788–794.
24. Walter TS, et al. (2005) A procedure for setting up high-throughput nanolitre crystallization experiments. Crystallization workflow for initial screening, automated storage, imaging and optimization. *Acta Crystallogr D Biol Crystallogr* 61(Pt 6):651–657.
25. Otwinowski Z, Minor W (1997) Processing of X-ray diffraction data collected in oscillation mode. *Methods in Enzymology Vol. 276: Macromolecular Crystallography*, eds Carter CW, Sweet RM (Academic, New York), pp 307–326.
26. Hewat EA, et al. (1997) Structure of the complex of an Fab fragment of a neutralizing antibody with foot-and-mouth disease virus: Positioning of a highly mobile antigenic loop. *EMBO J* 16(7):1492–1500.
27. McCoy AJ, et al. (2007) Phaser crystallographic software. *J Appl Cryst* 40(Pt 4):658–674.
28. Emsley P, Cowtan K (2004) Coot: Model-building tools for molecular graphics. *Acta Crystallogr D Biol Crystallogr* 60(Pt 12 Pt 1):2126–2132.
29. Adams PD, et al. (2010) PHENIX: A comprehensive Python-based system for macromolecular structure solution. *Acta Crystallogr D Biol Crystallogr* 66(Pt 2):213–221.
30. De Colibus L, et al. (2014) More-powerful virus inhibitors from structure-based analysis of HEV71 capsid-binding molecules. *Nat Struct Mol Biol* 21(3):282–288.
31. Zhu L, et al. (2015) Structure of Ljungan virus provides insight into genome packaging of this picornavirus. *Nat Commun* 6:8316.
32. Walter TS, et al. (2012) A plate-based high-throughput assay for virus stability and vaccine formulation. *J Virol Methods* 185(1):166–170.
33. Shu P-Y, et al. (2003) Development of group- and serotype-specific one-step SYBR green I-based real-time reverse transcription-PCR assay for dengue virus. *J Clin Microbiol* 41(6):2408–2416.
34. Livak KJ, Schmittgen TD (2001) Analysis of relative gene expression data using real-time quantitative PCR and the 2(-Delta Delta C(T)) Method. *Methods* 25(4):402–408.
35. Mastronarde DN (2005) Automated electron microscope tomography using robust prediction of specimen movements. *J Struct Biol* 152(1):36–51.
36. Li X, et al. (2013) Electron counting and beam-induced motion correction enable near-atomic-resolution single-particle cryo-EM. *Nat Methods* 10(6):584–590.
37. Kivioja T, Ravantti J, Verkhovsky A, Ukkonen E, Bamford D (2000) Local average intensity-based method for identifying spherical particles in electron micrographs. *J Struct Biol* 131(2):126–134.
38. Ludtke SJ, Baldwin PR, Chiu W (1999) EMAN: Semiautomated software for high-resolution single-particle reconstructions. *J Struct Biol* 128(1):82–97.
39. Zhang K (2016) Gctf: Real-time CTF determination and correction. *J Struct Biol* 193(1):1–12.
40. Scheres SH (2012) RELION: Implementation of a Bayesian approach to cryo-EM structure determination. *J Struct Biol* 180(3):519–530.
41. Tang G, et al. (2007) EMAN2: An extensible image processing suite for electron microscopy. *J Struct Biol* 157(1):38–46.
42. Pettersen EF, et al. (2004) UCSF Chimera—A visualization system for exploratory research and analysis. *J Comput Chem* 25(13):1605–1612.
43. Chen VB, et al. (2010) MolProbity: All-atom structure validation for macromolecular crystallography. *Acta Crystallogr D Biol Crystallogr* 66(Pt 1):12–21.
44. Xiao C, Rossmann MG (2007) Interpretation of electron density with stereographic roadmap projections. *J Struct Biol* 158(2):182–187.
45. Kucukelbir A, Sigworth FJ, Tagare HD (2014) Quantifying the local resolution of cryo-EM density maps. *Nat Methods* 11(1):63–65.
46. Ashkenazy H, Erez E, Martz E, Pupko T, Ben-Tal N (2010) ConSurf 2010: Calculating evolutionary conservation in sequence and structure of proteins and nucleic acids. *Nucleic Acids Res* 38(Web Server issue):W529-33.
47. Larkin MA, et al. (2007) Clustal W and Clustal X version 2.0. *Bioinformatics* 23(21):2947–2948.
48. Gouet P, Courcelle E, Stuart DI, Métoz F (1999) ESPript: Analysis of multiple sequence alignments in PostScript. *Bioinformatics* 15(4):305–308.